

Presented at the 27th Leeds-Lyon Symposium on Tribology, Tribological Research: From Model Experiment to Industrial Problems: Mechanics, Materials Science, Physico-chemistry Lyon, France, September 5, 2000

First Principles Multiscale Modeling of Physico-Chemical Aspects of Tribology

William A. Goddard III*, Tahir Cagin, Yue Qi, Yanhua Zhou, Jianwei Che

Materials and Process Simulation Center, 139-74, Division of Chemistry and Chemical Engineering, California Institute of Technology, Pasadena, CA 91125, USA

We have been developing methods to obtain a fundamental understanding of the physico-chemistry of sliding systems in contact that underlies the materials science and mechanics issues essential to tribology. Advances in theory and methods are now making it practical to consider fully first principles (de novo) predictions of surface and interface structures and their role in determining tribological properties of materials. Despite the progress, there remains an enormous gap between the distances and time scales of quantum mechanics (QM) simulations and the quantitative macroscopic continuum models essential in engineering design of tribosystems.

In order to bridge this gap, we use a hierarchy of simulations, beginning with QM, continuing through Molecular Dynamics (MD), then to mesoscale dynamics, to continuum mechanics, and finally to engineering design. A recent advance here is the development of first principles Force Fields (FF) based on QM that allow MD to describe bond breaking, plasticity, and phase transitions. Such FF are being used to extract mesoscale parameters for describing the dislocations for metals and their role in plasticity. Based on these FF, we used steady state nonequilibrium MD (NEMD) to study Crack Initiation and Spallation failure in such systems.

We illustrate the atomistic approach to tribology of metal surfaces by determining the shear and friction for Ni(001)/Ni(001) as a function of misorientation. These results suggest that some degree of plasticity occurs even for careful experiments on clean samples.

We illustrate the use of NEMD to study the rheology of confined lubricants, considering a system of two oxidized iron surfaces, covered with DTP wear inhibitors, and lubricated with hexadecane. These results illustrate the dramatic effects of nanoconfinement.

We illustrate the use of bond dissociation consistent FF, by examining the use of nanotubes as nanotribological probes.

*To whom correspondence is to be addressed, Email: wag@wag.caltech.edu

1. INTRODUCTION

In order to develop new materials with improved tribological performance, it is essential that their properties be predicted accurately before preparation, processing, and experimental characterization. Despite the tremendous advances made in the modeling of the structural, thermal, mechanical, and transport properties of materials at the macroscopic level (finite element analysis of complicated structures), there remains tremendous uncertainty about how to predict many critical properties related to performance. The fundamental problem here is that these properties depend on the atomic level interactions and chemistry (e.g., making and breaking

of bonds) requiring a description of the electronic states and forces at the level of nanometers and picoseconds, while the materials designer needs answers from macroscopic modeling (finite element paradigm) of components having scales of cm and milliseconds or larger. To dramatically advance the ability to design useful high performance materials, it is essential that we insert the chemistry into the mesoscopic and macroscopic (finite element) modeling.

The difficulties in doing this are illustrated in Figure 1, where we see that vast length and time scales separate Quantum Mechanics (QM) from the macroscopic world of engineering design.

Tremendous advances have been made recently in first principles QM predictions of chemical reactions, but the state of the art can handle accurately reactions with only ~100 atoms. There is no practical approach to carrying out a QM calculation on the initiation and propagation of a crack at a rolling contact. Despite this difficulty, *the computations MUST be based on accurate first-principles quantum mechanics if we are to predict the properties of new tribosystems*

Our **strategy** for accomplishing this objective is to develop an overlapping hierarchy of successively coarser modeling techniques description, as illustrated in Figure 1, where at each plateau (a range of length and time scales) the parameters of the coarse description are determined from first principles based parameters of the immediately finer level. For example, based on accurate QM calculations we find a Force Field (FF) including charges, force constants, polarization, van der Waals interactions etc. that accurately reproduces the QM. With the FF, the dynamics is described with Newton's equations [Molecular Dynamics (MD)], instead of the Schrödinger Equation. The MD level allows one to predict the structures and properties for systems $\sim 10^4$ to $\sim 10^5$ times larger than for QM, allowing direct simulations for the important properties of many interesting systems. This leads to many results relevant and useful in materials design; however, many critical problems in materials design require time and length scales for too large for practical MD.

Thus we are also developing methods to describe the mesoscale lying between the atomic length and time scales of MD and the macroscopic length and time scales (microns to mm and μsec to sec) of Finite Element Analysis (FEA). This linking through the mesoscale in which we must describe the microstructure is probably the greatest challenge to developing reliable first principles methods for practical materials design applications. Only by establishing this connection from microscale to mesoscale will it be possible to build first principles methods for describing the properties of new materials and composites (the domain of materials science and engineering) in terms of fundamental principles of physics and chemistry. Thus, for fundamental prediction to play a direct role in materials innovation and design, it is essential to bridge the micro-meso gap. We will illustrate this with examples of extracting the mesoscale parameters describing dislocations (Peierls Forces, kink formation). In addition, we show some direct simulations of crack propagation and spallation failure.

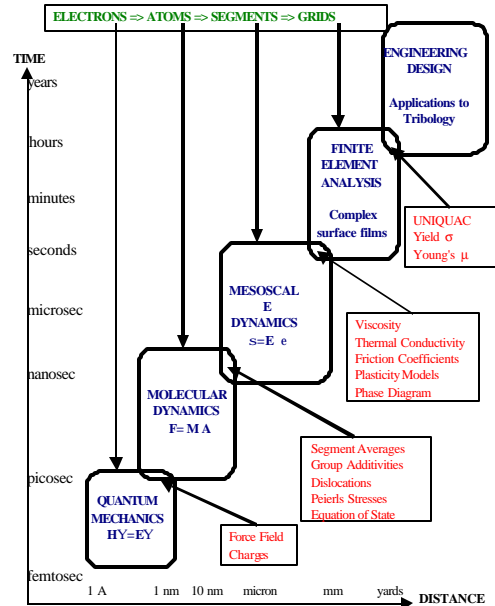


Figure 1 Multiscale modeling hierarchy for TriboSimulations. Tribology demands first principles simulations because essential parameters are not available from experiment. First Principles implies using Quantum Mechanics (QM) but QM is practical only for 100's atoms. Thus first principles TriboSimulations require that we use an overlapping hierarchy of methods to connect QM with engineering systems. We use QM to define the Force Field (FF) and then use this FF in Molecular Dynamics (MD) on systems large enough (up to millions of atoms) to describe good models for the tribosystem. This can allow numerical experiments to determine the essential elements of the behavior of the tribosystem, including constitutive equations. We can also extract parameters and elements for mesoscale simulations (for example, Peierls stresses for dislocation migration).

As these simulation methods are developed and made easy to apply, we expect a revolution in materials design applications where the use of first principles multiscale simulations allows an every increasing amount of the design to be done on the computer before experiment

2. Simulation Methodology

2.1. Quantum Mechanics Density Functional Theory Applications¹⁻⁴

Our strategy for obtaining accurate FF for TriboSimulations is to first use QM to calculate the equation of state of the materials over a range of

pressures ranging from ~ 500 GPa (compression) to ~ -10 GPa (tension) and to consider also defects such as vacancies over a similar range of pressure. We carry out these calculations for a variety of phases chosen to model the different coordinations that might be found in the material under various circumstances. In addition, we calculate the phase transitions between some of the phases.^{5,6} These calculations require a description of infinite systems using periodic boundary conditions (PBC). This is three-dimensional (3D) for bulk properties or two-dimensional (2D) for surface growth and interfaces. The most practical approach to such QM calculations is to use Density Functional Theory (DFT). There are various flavors of DFT, but for our purposes, it is *not* adequate to use the simplest approach, Local Density Approximation (LDA). It is essential to include gradient corrections (the Generalized Gradient Approximation). Such PBC calculations can be carried out either using plane wave basis sets (the most common approach) or using the Gaussian basis functions standard for finite systems. We used plane waves in the QM studies for determining the FF reported here. In most calculations on transition metal systems and larger main group elements, Effective Core Potentials are used to replace the core electrons while properly including the effect of the Pauli Principle. In some cases, the exact core orbitals are included and the plane waves are orthogonalized to them. We have used both approaches.

2.2. Force Fields (FF)

Based on the QM results we develop FF to provide the energies and forces needed for simulating nanophase materials and their properties. The FF must even be accurate enough to describe the phase behavior of the materials and transferable so that one can apply it to interfaces between different materials. Common FF use simple springs to represent bonds and angles in describing structures and vibrations of molecules. Such general FF are often not sufficient to accurately describe the detailed properties of specific molecules or polymers. For better FF, we fit to the QM using the Hessian-Biased FF (HBFF)⁷ approach, which combines normal mode information from HF theory with the frequency information from theory or experiment. This HBFF approach has been used to develop accurate FF for polymers (e.g., PE, PVDF, nylon, POM, SiH)⁸⁻¹³, ceramics (e.g., Si₃N₄, C₃N₄)^{14,15} semiconductor¹⁶ and metals.¹⁷

On the other hand, for fast qualitatively considerations of new systems, we find that generic FF suitable for general classes of systems are most useful. Examples include the DREIDING¹⁸ (for the main group elements) and the Universal force field

(UFF)¹⁹ (all elements, including inorganics and organometallics). For predicting the surface and interface properties of materials essential to describe the friction and wear mechanisms in materials, we believe that it is essential to use accurate environment dependent reactive force fields derived from first principles. In recent years critical advances have been made in using QM results to develop accurate FF for describing

a) metals where many-body interactions play critical role on their physical properties;^{20,21} in these force fields we have described cohesion in metals through many body interactions or through an embedding energy. The parameterization of the force fields is based on DFT level quantum mechanical calculations on pure metals.

b) oxides, ceramics, and zeolites where competition between ionic and covalent bonding is often very important, especially in describing polymorphic phase transitions, reactions, surface and interface properties.²²⁻²⁵ Here, we have used a Morse stretch two body pairwise interaction to account for short-range interactions, whereas the electrostatic interactions are environment dependent. The charges of the ions are assumed variable and reevaluated at each configuration using charge equilibration.

c) covalent-bonded system (such as carbon, hydrocarbons, silicon, and germanium) where the description of bond breaking and forming must be a part of an accurate classical description.²⁶⁻²⁷ Bond order dependent force fields are truly reactive force fields and extremely useful in studying the friction and wear properties of such systems.

2.3 Molecular Mechanics and Molecular Dynamics: MPSim

Using these force fields (FF) in large-scale Molecular Dynamics simulations allows practical calculations on up to several millions of atoms. Our methods take advantage of evolving hardware and software technologies to extend the time and distance scale to 100s of ns and close to microns. This involves using fast multi-pole techniques, multiple time step approaches, NEIMO (Newton Euler Inverse Mass Operator) constrained MD methods, and nonequilibrium MD approaches where they are suitable.

Thus, we have extended the methods of MD to physical systems of molecules, polymers, liquids, and inorganic materials with up to 100 million atoms while accurately treating long-range interactions using the cell multipole method (CMM). For fast internal coordinate dynamics on a million atoms, we have developed the Newton-Euler Inverse Mass Operator (NEIMO) method. This methodology handles periodic systems and extended Gibbs-

Ensemble molecular dynamics. These methods enable us to investigate the long time dynamics of liquid polymer and solid interfaces; to study such technological applications; as wetting, adhesion, phase separation, coatings.

In MD simulations, the FF is used to predict the equations of motion. This leads to trajectories $[\mathbf{x}_i(t), \mathbf{v}_i(t); \dots = 1, \dots, 3N]$ that can be analyzed (using statistical mechanics and thermodynamics²⁸⁻²⁹ principles) to obtain macroscopic properties. MD simulations of heterogeneous nano-phase materials may require millions of atoms to be considered explicitly (a 25 nm cube of polyethylene has 1 million atoms). The most time-consuming aspect of the MD simulations of large systems is the accurate evaluation of the long-range interactions (electrostatic and dispersion), which decrease slowly with distance. Without cutoffs, this cost scales as order (N^2) for N particles (a system of 10 million atoms leads to 10^{14} terms to be evaluated each step). However, cutoffs can lead to excessive errors. For a periodic system, the Ewald procedure leads to accurate summations for these interactions, but the problem scales as $N^{1.5}$, totally impractical for systems with million atoms.³⁰⁻³¹ In order to simulate systems with millions of atoms, we developed methods and optimized parallel computer programs efficient for high capacity MD with the following advanced features:

i. Cell Multipole Method³² (CMM) which dramatically reduces the cost of long-range Coulomb and van der Waals interactions while retaining high accuracy. The cost scales linearly with size, allowing MD simulations for million atom systems.³³⁻³⁵

ii. Reduced Cell Multipole Method³⁶ (RCCM) which handles the special difficulties with long-range Coulomb interactions for crystals by combining a reduced unit cell plus CMM for interaction of the unit cell with its adjacent cells. The cost scales linearly with size while retaining high accuracy, allowing simulation of crystals having a million atoms per unit cell (the major use is for models of amorphous and semi-crystalline materials).

iii. Newton Euler Inverse Mass Operator method (NEIMO)³⁷⁻⁴⁰ for internal coordinate dynamics (e.g., treats torsions only). This allows the solution of the dynamical equations for internal coordinates without inverting the mass tensor (moment of inertia tensor). The cost of NEIMO is linear in the number of degrees of freedom and small compared to other costs for million atom systems. More recently we also developed a new constrained force algorithm (CFA) for massively parallel MD simulation of polymers and dendrimer.^{39,40}

iv. Advanced MD algorithms to simulate systems under constant temperature and constant pressure conditions.⁴¹⁻⁴⁵

v. Nonequilibrium MD: We have implemented synthetic equations of motions to simulate various nonequilibrium conditions to predict transport properties such as viscosity, thermal conductivity of materials.⁴⁶⁻⁴⁸ Using these methods, we have studied the effect of molecular topology of liquid alkanes on their measured viscosity indices⁴⁹.

vi. Steady State MD Methods are used to simulate non-equilibrium processes such as friction and wear in molecularly confined lubricants and diamond surfaces. Here, the external work is dissipated through the material and coupled to a thermal bath using the Langevin equation.⁵⁰⁻⁵² This method is specifically developed for studying tribological properties of materials.

In the next three sections, we will outline three recent applications relevant to tribology:

3. Application of MD to Studying the Misorientation on the Friction Between two Ni (100) Surfaces

Stimulated by recent experiments by Gellman and coworkers,⁵³ we carried out simulations of the friction at between two clean Ni surfaces being rubbed against each other. In particular we examined the effect of orientation on both the dynamic and static coefficient of friction.

3.1 Introduction

Figure 2 shows the experimental results from Gellman and Ko⁵³ for the friction Anisotropy at the interface of clean Ni (100) and misoriented clean Ni (100). These Experiments of the static coefficient of friction on clean surfaces show that commensurate (0°) and incommensurate interfaces lead to similar results $\mu \sim 7$, except for 45° , where it decreases by 50%. This is in conflict with the analytic theories which suggest that the large static friction on the commensurate interfaces and no static friction on the clean incommensurate surfaces, due to the lack of periodicity.⁵⁴⁻⁵⁵ Robbins et al. studied similar phenomena and proposed a simple model that the absorption of “third body”, such as small hydrocarbon molecules, can cause the static friction of two macroscopic objects.⁵⁶ But the experiments were carried out in a highly controlled ultrahigh vacuum environment (UHV) and carefully showed that no impurities are present on the surface (as measure by AES) and that the surfaces were well ordered (as measured by LEED).

Figure 2. Experimental results on the friction Anisotropy at the interface of clean Ni (100) and misoriented clean Ni (100). [From Gellman and Ko, Langmuir, to be published]. Here the arrows indicate $\mu_s > 5.5$

Friction Between Clean Ni(100) Surfaces versus Lattice Misorientation

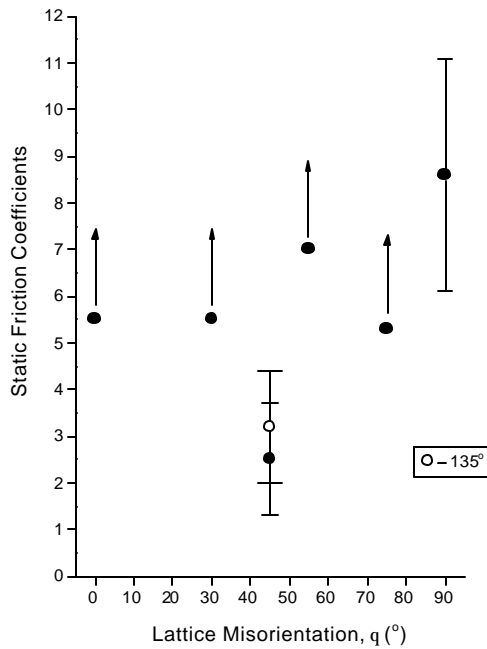
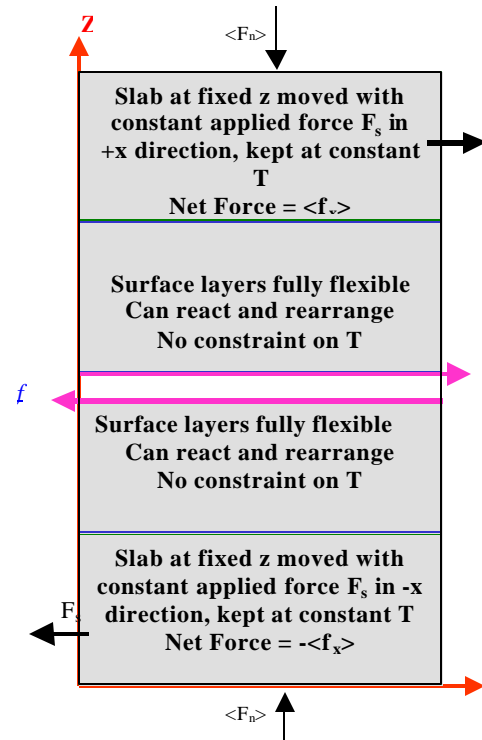


Figure 3. 2D Periodic Cell for Tribo-Simulations (Steady State Molecular Dynamics). A rigid slab of $N_f = 6$ layers of atoms is defined at the top and bottom in which all atoms move as a unit. At each time step, each atom in the rigid slab has imposed an external force of F_s/N where the force is in the $+x$ direction for the top slab and the $-x$ direction for the bottom slab. The outermost one layer in each rigid slab is constrained not to move in the z direction. The central two slabs, each with $N_f = 1$ layer of atoms, are fully flexible and allowed to move freely under the force field. The rigid slabs are thermostated to a fixed temperature $T=300K$. The flexible slabs are treated adiabatically. The normal force $\langle F_n \rangle$ is summed over all atoms of the top two slabs and averaged over time, which is equal in magnitude and opposite in sign to the normal force on the bottom two slabs. The total lateral force on the top two slabs is calculated as $\langle f_x \rangle$, which is equal and opposite to the lateral force on the bottom two slabs. The frictional force f is defined as $f = F_s - \langle f_x \rangle$. Thus the Dynamic Friction coefficient is defined as $\mu_d = 2f / \langle F_n \rangle$. F_c is the minimum force needed to initiate motion. Thus the static friction coefficient is defined as $\mu_s = 2F_c / \langle F_n \rangle$.



In order to examine the origin of these surprising results, we carried out a series of Non Equilibrium Molecular Dynamics (NEMD) calculations designed to mimic the experimental conditions. The details of the calculations are described in section 2 and the results are presented in section 3. The significance of the current results and future plans are discussed in section 4.

3.2 Computational Details

For the Force Field (FF) we use the quantum Finnis-Sinclair (Q-FS) type many-body force field which has previously been used to study structural transitions between various phases of Ni, Cu and other face centered cubic metals. The parameters for this FF were determined to match the experimental properties of bulk Ni (density, cohesive energy, compressibility, elastic constants, and phonon dispersion). In doing the fit, we included the zero point motion of the vibrations.²⁰⁻²¹ This Q-FS FF has previously been used to study structural transitions between various phases of Ni, Cu and other face centered cubic metals.⁵⁷⁻⁵⁹

Figure 3 shows the y projection of a 2D Periodic Cell (x, y periodic, z non-periodic) used for the Steady State NEMD Tribo-Simulations. In all the models, there are 7 layers of atoms in both slabs. A rigid slab of $N_r = 6$ layers of atoms is defined at the top and bottom in which all atoms move as a unit. At each time step, each atom in the rigid slab has imposed an external force of F_s where the force is in the +x direction for the top slab and the -x direction for the bottom slab. The top layer in the top rigid slab and bottom layer in the bottom slab are constrained not to move in the z direction, such that the sample is fixed length on z direction. The central two slabs, each with $N_f = 1$ layer of atoms, are fully flexible and allowed to move freely under the force field. The rigid slabs are thermostatted to a fixed temperature $T=300K$ (iso-kinetic energy). The flexible slabs are treated adiabatically. The normal force $\langle F_n \rangle$ per atom is calculated from the average stress times the contact area and divided by the number of atoms, since the sample is under compression. The average of lateral force per atom on the top rigid slab is calculated as $\langle f_x \rangle$, which is summed over all atoms of the top rigid slab and averaged over time, and is equal and opposite to the lateral force on the bottom rigid slab. Notice that the average atomic net forces $\langle f_x \rangle$ in the upper and lower slabs are not equal to applied force, after two pieces started to move. The difference is the frictional force, f , at the interface.

$$f = F_s - \langle f_x \rangle \quad (1)$$

We validated that the relative acceleration of two bodies is due to the net force, which means $a=2\langle f_x \rangle/m$. Thus, the Dynamic Friction coefficient is defined as

$$\mu_d = 2f/\langle F_n \rangle. \quad (2)$$

F_c is the minimum force needed to initiate motion. Thus, the static friction coefficient is defined as

$$\mu_s = 2F_c / \langle F_n \rangle. \quad (3)$$

We have examined here the effect of orientation on both the dynamic and static coefficient of friction for two orientations of the bottom surfaces with respect to the top:

- $\theta=0^\circ$ corresponds to the case where both surfaces are aligned. This system is expected to have a very high coefficient of friction, particularly for the static, perfect case. In this case, the direction of sliding is taken as the $\langle 110 \rangle$ direction for both slabs, as the same as the experiment.
- $\theta=45^\circ$ corresponds to the case of the maximally mis-oriented surface, where the $\langle 110 \rangle$ axis of the lower surface matches the $\langle 100 \rangle$ direction of the top surface. In this case, the direction of sliding is taken as the $\langle 100 \rangle$ direction of the upper slab. The mis-orientation causes the lattice mismatch too. In this case we choose $10a \times 10a$ for lower slab, and $7\sqrt{2}a \times 7\sqrt{2}a$ for upper slab then stretch it to 1% tension strain to reach $10a$ length.

We examined two surface structures.

- The Perfect Interface, where each surface is atomically flat and clean. However, the surfaces start with the atoms of the top and bottom surface aligned. Thus, these layers are slipped with respect to a single crystal.
- The Rough interface where 25% of the atoms at the interface of each surface were randomly deleted. Here the top and bottom surfaces were treated individually. The same rough surfaces were used for both orientations.

Before the sliding simulation, we first prepare the sample by relaxing the up and lower pieces of Ni for 20ps at 300K respectively to reach equilibrium then bringing two pieces of material together for another 20ps relaxation. During the relaxation, constant temperature and constant volume molecular dynamics (ThN MD) was used and the sample is non-periodic along z-axis, but periodic along x and y directions.

The unit of force is $(kJ/mol)/nm/atom = 1.66 \cdot 10^{12} N/atom$

3.3 Results

The various cases considered here are summarized in Table 1.

3.3.1 Perfect Interface ($q=0^\circ$ and $q=45^\circ$)

Figure 4 shows the Displacement in x direction of upper slabs for the Ni (100)/Ni(100) perfect interface. The upper curve is for the $\theta=45^\circ$ misorientation, while the lower curve is for perfect alignment ($\theta=0^\circ$). Here F_s is the applied force to the rigid slabs. For $\theta=0^\circ$ we see that $F_s = 15$ and lower leads to oscillatory motion, indicating that this force is less than F_c . Clearly the friction is much less for the misoriented surface than for $\theta=0^\circ$.

Figure 5 shows a snapshot of the atomic structure of the systems whose performance is plotted in Figure 4. The Upper curve is for $\theta=45^\circ$ misorientation with an applied force of $F_s=0.255$ after 10ps. The Lower curve is for perfect alignment ($\theta=0^\circ$) with $F_s=20.17$ after 5ps. Even for the perfect surface, there is already some disorder. In addition there is plastic deformation for the case with perfect alignment. Clearly the static frictional force is much less for the

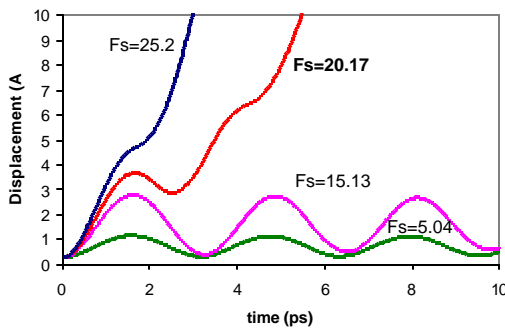
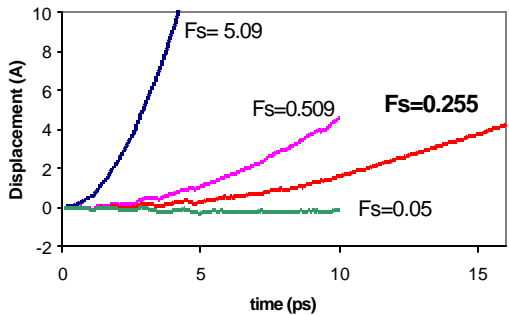
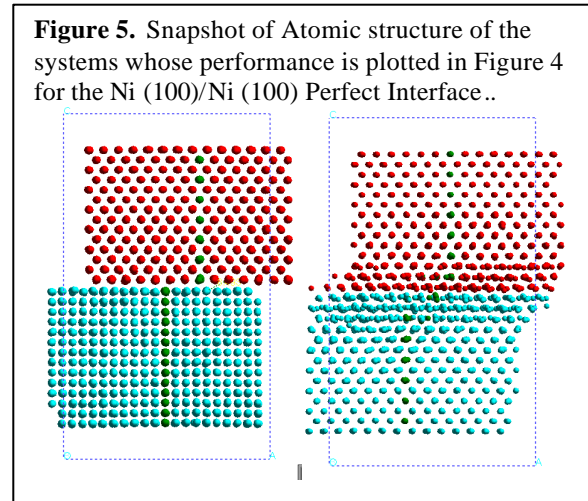


Figure 4. Displacement in x direction of upper slabs for Ni (100)/Ni (100) Perfect Interface. Upper curve for $\theta=45^\circ$ misorientation, lower curve for perfect alignment ($\theta=0^\circ$).

misoriented surface than for $\theta=0^\circ$. In the perfect alignment case, we found that the two pieces of the

materials collapsed into one piece, just as observed for Ni(100) by using equivalent crystal method [57]. As a result sliding requires shearing the perfect crystal, leading to very high friction. This was also found experimentally. When cold-welding occurred at the interface, the shear force was so large that it approached the upper limit of the tribometer, requiring terminating the experiment. Thus even for the perfect surface, there is already some disorder leading to plastic deformation during sliding for the case with perfect alignment. On the other hand the case with $\theta=45^\circ$, two flat surfaces keep atomic flat during sliding.



3.3.2 Rough Interface ($q=0^\circ$ and $q=45^\circ$)

Figure 6 shows the displacement in x direction of upper slabs for the Ni (100)/Ni(100) Rough Interface. The Upper curve is for the $\theta=45^\circ$ misorientation, the lower curve is for perfect alignment ($\theta=0^\circ$). For $\theta=0^\circ$ we see that $F_s = 10$ and lower leads to oscillatory motion, indicating that this force is less than F_c . Clearly the friction is less for the misoriented surface than for $\theta=0^\circ$.

Figure 7 shows a snapshot of the atomic structure of the systems whose performance is plotted in Figure 5 for the Rough Interface. Upper curve is for $\theta=45^\circ$ misorientation with an applied force of $F_s=2.25$ after 10ps. Lower curve is for perfect alignment ($\theta=0^\circ$) with $F_s=12.6$ after 6ps. Clearly the rough surface leads to disorder and wear even for $\theta=45^\circ$.

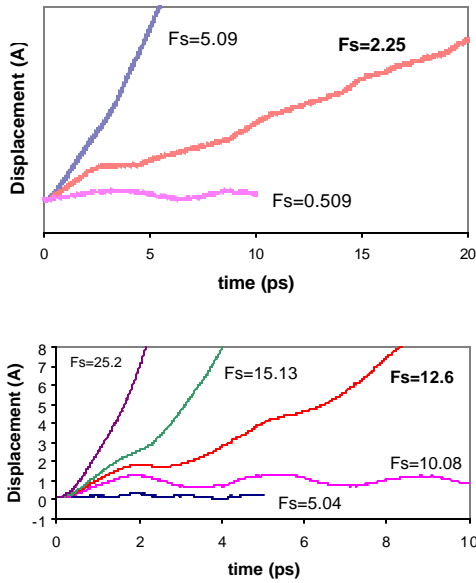
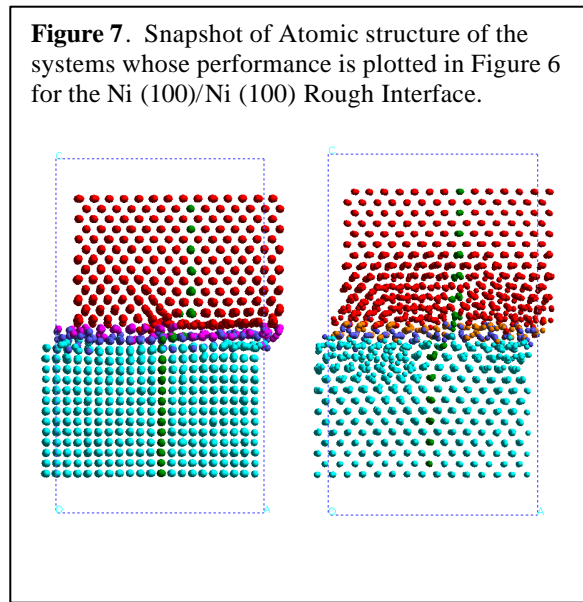


Figure 6. Displacement in x direction of upper slabs for the Ni (100)/Ni (100) Rough Interface. To make the Rough interface 25% of the atoms at the interface were randomly deleted. The Upper curve is for $\theta=45^\circ$ mis-orientation, while the lower curve for perfect alignment ($\theta=0^\circ$). F_s is the applied force to the rigid slabs.



3.4 Discussion

For $\theta=0^\circ$ the dynamic results lead to

- $\mu_d \sim 5.5$ for the perfect surface and
- $\mu_d \sim 8.3$ for the rough surface

whereas for the $\theta=45^\circ$ case for the dynamic case, we obtain

- $\mu_d \sim 2.5$ for the perfect surface and
- $\mu_d \sim 5.7$ for the rough surface

In the experimental dynamic friction coefficient was not reported, but the authors indicated that it would not change the overall conclusions based on the static frictional coefficient, regarding the orientation dependence of friction. The calculated static and dynamic friction coefficients are both close to the experimentally measurement values. The values from the simulations are comparable to the experimental values :

- $\mu_s \sim 8.5 \pm 2.5$ for the $\theta=0^\circ$ case and
- $\mu_s \sim 2.5 \pm 1$ for the $\theta=45^\circ$ case.

Indeed even the experimentally observed factor of two drop from $\theta=0^\circ$ to $\theta=45^\circ$ is captured by the dynamics calculations for the perfect case.

For The static case with $\theta=0^\circ$ the theory leads to

- $\mu \sim 14$ for the perfect surface and
- $\mu \sim 18$ for the rough surface

while with $\theta=45^\circ$ the theory leads to

- $\mu \sim 0.4$ for the perfect surface and
- $\mu \sim 4$ for the rough surface

The static friction coefficient on perfect misoriented interface is very low compared to 0 degree alignment case, which agrees with the analytic theories that there is no static friction (at least very low) on clean incommensurate interfaces. However, these values are not in agreement with the experiment for static μ on a perfect surface. Gellman and Ko were extremely careful to ensure that there are no impurities on the surface (as measured by AES) and that the surfaces were well ordered (as measured by LEED). However, even so the surface constructed by mechanical polished surface and Ar ion cleaning in the ultrahigh vacuum environment, need not be absolutely flat on the atomic scale. Our simulations show that even roughness in just the top layer on the surface can increase the static friction coefficient on misoriented surface 10 times, but does not increase much the value for the commensurate interface.

This suggests another model of the origin of static friction: the roughness, disorder, and plastic deformation on the interface can lead to significant static friction for macroscopic objects.

The close correspondence between the dynamic values from theory with the “static” values for the experiments is tantalizing. We speculate that the experimental surfaces are probably more like our slightly disordered surfaces after doing the dynamic.

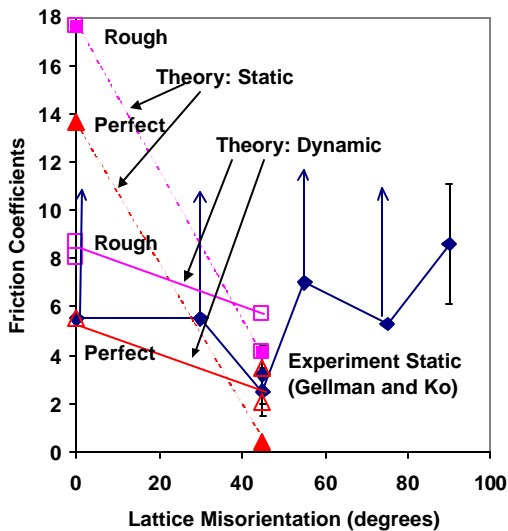
This suggests to us that the experimental surface might have disorder and other plastic deformation in the top layer, just as we find in the dynamics. We believe that disorder in just the top layer might still be compatible with the sharp LEED pattern observed experimentally. This suggests that in the theory the

surface must be rubbed (polished) to obtain surface like experimental “smooth surface.” If so then perhaps the theory and experiment are compatible. We are in the process of testing this hypothesis.

Table 1. Summary of results from NEMD simulations of friction on Ni (100)/Ni (100)

Orientation	Applied F_s	$\langle f_x \rangle$	Friction $f = F_s - \langle f_x \rangle$	$\langle f_n \rangle$ got from stress	velocity nm/ps or acceleration nm/ps ²	Friction Coefficients $\mu_s = 2F_s / \langle f_n \rangle$ or $\mu_d = 2f / \langle f_n \rangle$
Ni(0) perfect (110) (110)	5.04	0		0	v=0	
Ni(110) (110)	15.13	0.07	15.13	0.55	v=0	
Ni(110) (110)	20.17	3.035	17.14	2.95	a=0.09 $2\langle f_x \rangle / m = 0.10$	$\mu_s \approx 13.67$
Ni(110) (110)	25.2	7.59	17.61	6.36	a= 0.246 $2\langle f_x \rangle / m = 0.258$	$\mu_d = 5.54$
Ni(0) rough (110) (110)	5.04	0	5.04	0.52	v=0	
Ni (110) (110)	10.08	0	10.08	0.89	v=0	
Ni (110) (110)	12.6	0.62	11.98	1.43	v=0.1	$\mu_s = 17.6$
Ni (110) (110)	15.13	3.32	11.81	2.71	a=0.12 $2\langle f_x \rangle / m = 0.11$	$\mu_d = 8.71$
Ni (110) (110)	25.2	9.2	16	3.97	a=0.35 $2\langle f_x \rangle / m = 0.31$	$\mu_d = 8.06$
Ni(45) perfect (100) (110)	0.05	0	0.05	1.20	v=0	
Ni(100) (110)	0.255	0.130	0.125	1.19	v=0.082	$\mu_s = 0.428$
Ni(100) (110)	0.509	0.273	0.236	1.21	a=0.009 $2\langle f_x \rangle / m = 0.009$	$\mu_d = 0.39$
Ni(100) (110)	2.55	1.31	1.24	1.23	a=0.0487 $2\langle f_x \rangle / m = 0.045$	$\mu_d = 2.02$
Ni(100) (110)	5.09	2.96	2.13	1.22	a=0.111 $2\langle f_x \rangle / m = 0.101$	$\mu_d = 3.49$
Ni(45) rough (100) (110)	0.509	0	0.509	1.28	v=0	
Ni(100) (110)	2.55	0.06	2.49	1.24	v=0.25m/s	$\mu_s = 4.11$
Ni(100) (110)	5.09	0.75	4.34	1.52	a=0.025 $2\langle f_x \rangle / m = 0.026$	$\mu_d = 5.71$

Figure 8. Compare of calculated friction coefficients with experiment (Gellman and Ko, Langmuir) for the Ni (100)/(100) Surface. The experiment results are the filled diamonds, with arrows to indicate the range of values. The theory is denoted as triangles for perfect and squares for rough. Filled symbols are for the static case while open symbols are for the dynamic. We see that for the perfect surface the dynamic friction for $\theta=45^\circ$ is about half that for $\theta=0^\circ$. This is in excellent agreement with the “static” values from the experiment. For the rough surface the values are 25% larger for $\theta=0^\circ$ and twice as large for $\theta=45^\circ$, so that the ratio is about 80%. On the other hand, the “static” values from the theory lead to a large anisotropy, a factor of 5% for the perfect surface and 30% for the rough surface. The close correspondence between the dynamic values from theory with the “static” experiments suggests to us that the experimental surface might have disorder in the top layer, just as we find in the dynamics. This suggests that in the theory the surface must be rubbed (polished) to obtain surface like experimental “smooth surface.” We will test this in later calculations



4. Structural and Dynamic Properties of Lubricants Under Shear Flow in a Confined Geometry

4.1 Introduction

Motivated by developing environmentally compliant wear inhibitors we have studied the influence of self assembled organic additives on the rheology of lubricants.

Recent developments have led to an increasing understanding of fluids in ultra-thin films at the atomic scale.⁶⁰⁻⁶¹ Confining a liquid, by solid surfaces with atomistic scale separations leads to dramatic changes in physical properties.⁶²⁻⁶⁴ We report here an MD investigation of the dynamics for a nanoscale hexadecane film under the influence of a shear flow. The primary objective of the study is to enhance our understanding on how lubricants behave when they past engine surfaces and to assist in designing engine surfaces with reduced engine wear.⁶⁵⁻⁶⁷

The model of the present study builds upon our previous static studies of iron-oxide surfaces covered by a self-assembled monolayer (SAM) of adsorbed wear inhibitors (“brush”).⁶⁸ A lubricant film, namely liquid hexadecane, is sandwiched between two such protected iron-oxide surfaces. A planar flow is generated by moving the top surface and keeping the bottom surface stationary. Our model system consists of realistic lubricants, realistic solid surfaces, and realistic wear inhibitor molecules adsorbed on the surfaces.

The wear inhibitor molecules are dithiophosphates (DTP= $S_2P(OR)_2$, where R represents one of the three types of organic groups: R = isopropyl (iPr), isobutyl (iBu), and phenyl (Ph)).

4.2 Simulation Model

The details of simulations performed in this study are described in a recent paper,⁶⁹ which uses the model consist of a fluid consists of hexadecane molecules, $C_{16}H$ (32 per cell) with all C and H atoms considered using the DREIDING FF which is confined between two iron-oxide surfaces [modeled as $\alpha-Fe_2O_3$ with the (0001) cleavage plane perpendicular to z-axis] with four layers of atoms, each of which includes 16 Fe. The FF was developed to describe bulk $\alpha-Fe_2O_3$. Each of the surfaces is covered by 8 dithiophosphate (DTP) wear inhibitor molecules, which was calculated as the equilibrium coverage from MD simulations.

This was described with the DREIDING FF, modified to describe the vibrational frequencies correctly and with S-Fe vdW parameters determined from QM.

The system is maintained at $T = 500$ K. The lubricant and bottom layer started with the initial set of velocities from the Maxwell-Boltzmann distribution with center of mass velocity of zero. The top layer of the iron-oxide slab was sheared uniformly at the constant velocity while the bottom layer of the bottom slab was kept fixed. Thus a planar flow is generated in xz-plane. The other iron oxide layers, the DTP molecules, and the lubricant molecules are all described with full flexibility allowed to readjusting to the shearing motion until they attain a steady state shear velocity profile. We carried out ~ 200 ps of shear dynamics simulations. The time step is 1 fs.

The force field (FF) used in these calculation was obtained by combining the QM calculations on Fe-DTP clusters with the DREIDING force field¹⁸ to describe the DTP and iron oxide interactions. The derivation and the parameters for this FF were described elsewhere.⁶⁵⁻⁶⁶

The results presented below are from four different simulation runs:

- 1) R = iPr, $v = 1$ A/ps, and $H \sim 45$ A;
- 2) R = iBu, $v = 1$ A/ps, and $H \sim 45$ A;
- 3) R = Ph, $v = 1$ A/ps, and $H \sim 43$ A;
- 4) R = iPr, $v = 0.5$ A/ps, and $H \sim 20$ A.

Model system parameters are given in Table 2.

We observed distinct density oscillations, which is consistent with the previous work.⁶⁸ The density oscillations are quite significant near the walls (within 15 to 20 A). In the central region of the fluid, the layering decreases, with the density approaching to that of the bulk lubricant. For the separations of 44 A, we find 9-10 layers in the density. For the thinner system with just ~ 20 A separation (Figure 9d), we found 5 layers, but here the density oscillations are easily noticeable even in the central region of the film. In an earlier study⁶⁸ we have looked at the distribution of carbon atoms and that of hydrogen atoms separately. There we found that the distribution of hydrogen atoms is quite uniform and that the density oscillations are mostly resulted from the oscillation in the number density of carbon atoms. The viscosity of $C_{16}H_{34}$ was calculated for case a, with 4.5 nm thickness. The result is 5.6 times larger than calculated for the bulk liquid. This is comparable to an experimental observation by J-M Georges for hexadecane constrained to films of 5 nm, where a viscosity increase by a factor of ~ 5 was found compared to the bulk system.

For a comparison, we did a (static) simulation of 140-ps at zero shear velocity for the case of iPr with the exactly same setup.⁶⁸ There we still observed the strong density oscillations. From that, we concluded that the density oscillations observed in the lubricant films are induced by geometric confinement, rather than shearing.

Table 2. Values of the geometric parameters for the model system.

SAM	L^a (A)	H^b (A)	D^c (A)	h (A) ^d	Runtime (ps)
(I) 44 A Thick Film (shearing velocity 100 m/s)					
iPr	83.84	44.99	19.42	6.14	201
iBu	84.89	44.57	20.16	6.71	213
Ph	83.60	43.49	20.06	6.66	203
(II) 20 A Thick Film (shearing velocity 50 m/s)					
iPr	63.84	20.30	21.77	6.09	360

^a. Total length of periodic cell in z direction

^b. Thickness of the lubricant region.

^c. Thickness of the "brush" wall consisting of Fe_2O_3 and DTP monolayers.

^d. Thickness of wear inhibitor SAM.

4.3 Results and Discussions

4.3.1 Density Oscillations

4.3.2 Stick-Slip Motions

We further analyzed the contributions from each individual molecule to the oscillatory

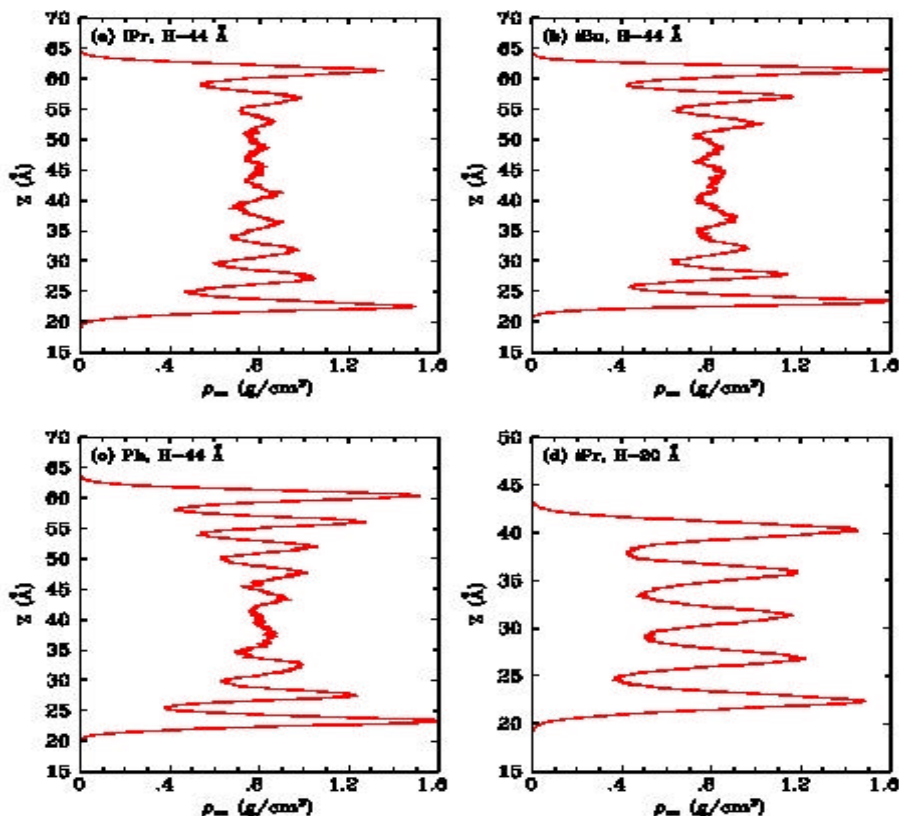
distribution of total carbon atoms in the lubricant film. The results are shown in Figure 11 for iBu where the carbon atom distribution for each of the 32 We can see *stick-slip* motion in the molecules near the bottom and top interface in all three cases. The stick-slip motion, often observed in macroscopic studies on solid surfaces,^{68,69} is characterized by a sequence of move (slip), pause (stick), and move (slip) again. The case of iBu shows the most regular character, with a periodicity of ~ 40 ps whereas the stick-slip motions for the iPr and Ph cases are more irregular.

Normally, in observing the stick-slip motion, the experimental setup is to place a solid sliding block on top of a solid surface and drive the top block elastically. Here, in our simulation, the top "brush" surface was driven smoothly at a constant velocity, and we observed the stick-slip motion in the bottom layers of the lubricant.

In this case the stick-slip motion of the interfacial boundary propagates into the lubricant.

What is the origin of the lubricant stick-slip motion? In the case of stick-slip sliding on solid surfaces, there is a one-to-one correspondence between the stick-slip motion and the frictional force or shear stress (the ratio of the frictional force to the contact area). The friction is highest during the stick period (referred as static friction) and lowest during the slip period (referred as kinetic or dynamic friction). We have evaluated the frictional forces in our systems, but unfortunately, the fluctuations of the friction forces themselves are so large that it is impossible to differentiate them from the difference between the static friction and kinetic friction.⁷⁰

Figure 9. The density distribution of the lubricant as a function of z (perpendicular to the surface). We used 1000 bins to count the number of Carbon atoms falling in a zone between z and $z+dz$ at each time-step. This density was averaged over the last 100 ps of the 200 ps runs: (a) iPr, $H \sim 45$ Å; (b) iBu, $H \sim 45$ Å; (c) Ph, $H \sim 43$ Å; and (d) iPr, $H \sim 20$ Å. Note that (d) is half the lubricant thickness as the others. The layering occurs within ~ 18 Å of the DTP SAM layer, leaving only about 9 Å of bulk lubricant for a, b, and c, but none for d.



Since the flow behavior of the lubricant changes dramatically with the nature of the wear inhibitor molecules at the interface, we concluded that the properties of the SAM molecules must play a role. Since the SAM molecules stay at the same relative position on the iron oxide surface, they probably play the role on modulating (elastically) the frictional forces on the lubricant. Thus, although the top wall is moving at a constant velocity, the wear inhibitor molecules lead to elastic response causing an oscillatory driving forces to the lubricant. That is, the lubricant might compress or push the SAM molecules, which then rebounds to press on the neighboring lubricant molecules.

4.3 Remarks

Here we found that in such a confined geometry, the lubricant films exhibit strong density oscillation. For the separations of 44 Å we found 9-10 layers in the density, and for a 20 Å separation we found 5 layers.

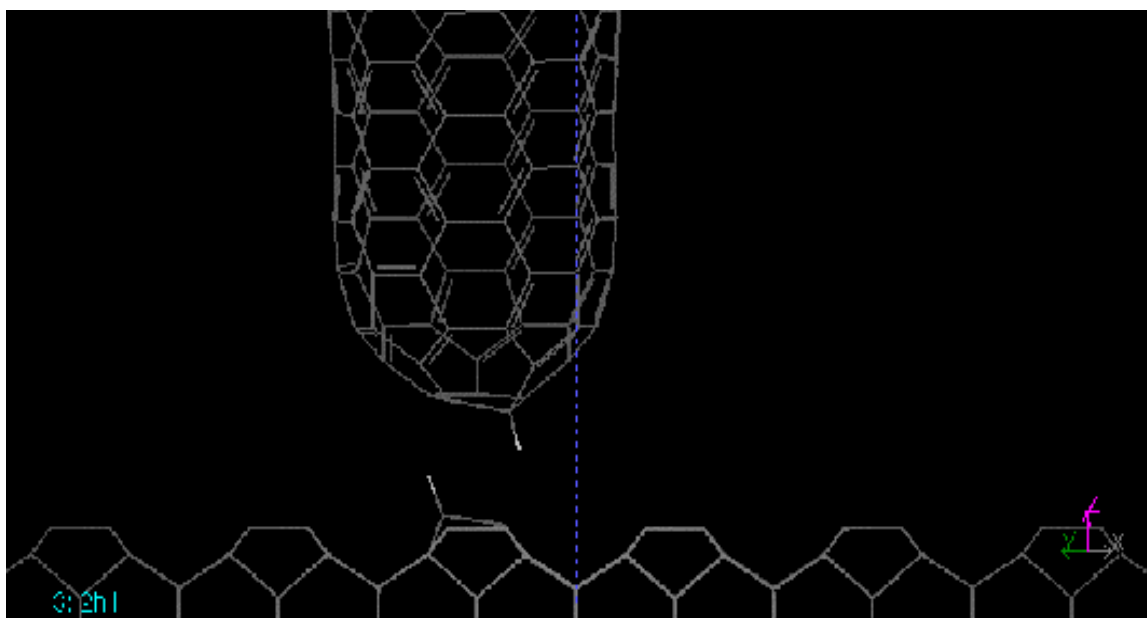
In addition, we found that the motion of each individual molecule in the direction perpendicular to the surfaces is very limited.

They are confined within 1-2 layers. Under a shear flow, the lubricant molecules near the bottom surface boundary show stick-slip motion in the shear direction. However, the stick-slip motion cannot be simply characterized by the stretching or compressing of molecule. The characteristics of stick-slip motion is very sensitive to the type of "brush" molecules on the surfaces that are in direct interactions with the lubricant molecules. The stick-slip motion should disappear on an ideally smoothed surface.

5. Carbon Nanotube as a Tribological Probe

Carbon nanotubes possess unique electronic and mechanical properties providing the promise of very interesting applications in nanotechnology. Recently, nanotubes have been used in Atomic Force Microscope (AFM) experiments that indicate significant advantages due to the 1 nm length scale, mechanical strength, and stability/reversibility. Large quantities of carbon nanotubes have become available commercially, but their remain challenges to synthesize and pack nanotube into ordered arrays.

Figure 10. Configuration of functionalized nanotube tip and active site of diamond reconstructed surface (100).

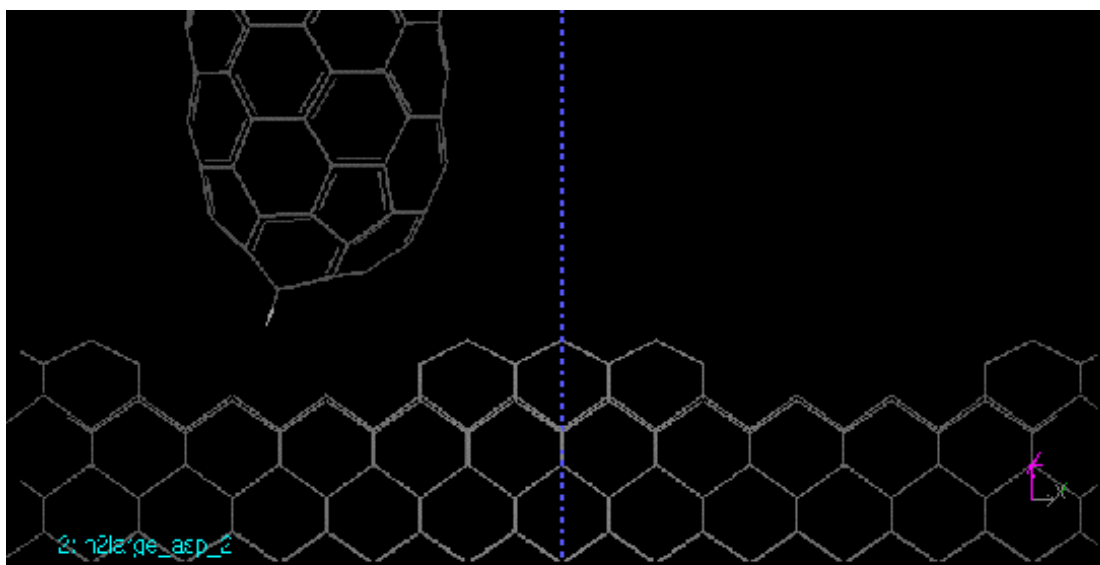


Our interest here is the use of nanotubes to probe issues of friction and wear at a molecular level, where the macroscopic rules of friction resulting from statistical averaging need not hold. Thus at the molecular level, wear involves chemical reactions, which bonds breaking and atoms being transferred from one surface to another. In order to address the relationship between the molecular level surface structure and the nanoscale friction behavior, it is necessary to design new experiments that can simultaneously probe the surface structure and the atomic friction at the nanometer scale. We suggest that the unique properties and structures of carbon nanotubes make them ideal candidates to achieve this goal. In order to illustrate this, we have carried out some computational experiments to indicate some of the properties.

atoms has one hydrogen atom attached, leading to a dangling bond orbital on the adjacent atom. By pushing down the nanotube tip, we can expect some chemical reactions between the tip and the diamond surface active site since both tube tip and surface have unpaired electrons. There are three possible reaction pathways:

- hydrogen extraction from the nanotube tip to the diamond surface,
- hydrogen extraction from the diamond surface to the tip, and
- bonding of the dangling bonds on the diamond surface to the graphene tip.

Figure 118 *Nanotube tip and rough diamond surface*



A very useful property of carbon nanotube is that the tube tip can be functionalized to provide active species that might for example be used to initiate surface reactions at a precise position. By measuring the force/energy on the nanotube, we can probe the details concerning the reaction between the tube tip and the surface. Thus, Figure 10 shows a simple example in which the nanotube tip is functionalized by a single hydrogen atom, leaving an unpaired electron to make this hydrogen very reactive. In Figure 10, this tip is pushed against the reconstructed (100) diamond surface. Here one of the paired surface

In addition to monitoring and probing chemical reactions on atomic surfaces Carbon nanotubes can also be used to probe the frictional behavior at an atomic scale of resolution without introducing chemical reactions. Figure 11 shows a specially constructed rough diamond surface that we used to test the sensitivity of the nanotube “tribology machine.” Here two atomic layers were removed periodically to obtain atomic scale asperities. As the nanotube is moved across the surface, it will feel stronger and weaker interactions as it encounters the hills

and valleys on the surface. It can simultaneously measure the forces both in the normal direction and lateral directions. The normal forces can be used to extract information about the surface pattern. Then the lateral forces, can be use to determine the friction. Figure 12 depicts the normal forces. Here the envelope of normal forces clearly reflects the surface roughness. Figure 13 shows lateral frictional forces. The high frequency oscillations in the lateral forces involve the atomic vibrational motions. Eliminating these with a low pass filter leads to a force envelope that very clear shows the stick-slip motion. From the averaged lateral forces and normal forces, it is possible to deduce the macroscopic friction coefficient. It can also be obtained by monitoring the energy dissipation.

Figure 14 shows the external energy consumed as a function of time during the process of nanotube movements. The energy curve illustrates both overall energy consumption due to friction between the tip and surface and detailed information about surface roughness. From the linear fit of the energy curve, we can deduce the effective friction coefficient, (this assumes that the friction coefficient does not vary appreciably for different speeds in tip movements). We find that the friction coefficient calculated from the ratio between lateral force and normal force is ~ 0.25 as is the value calculated from the energy dissipation. Of course, the accuracy of the value depends on the accuracy of the atomic interactions (the Force Field).

Figure 12 Normal force acting on the nanotube tip. The black curve is the actual force, and the light smooth curve is the Fourier filtered force.

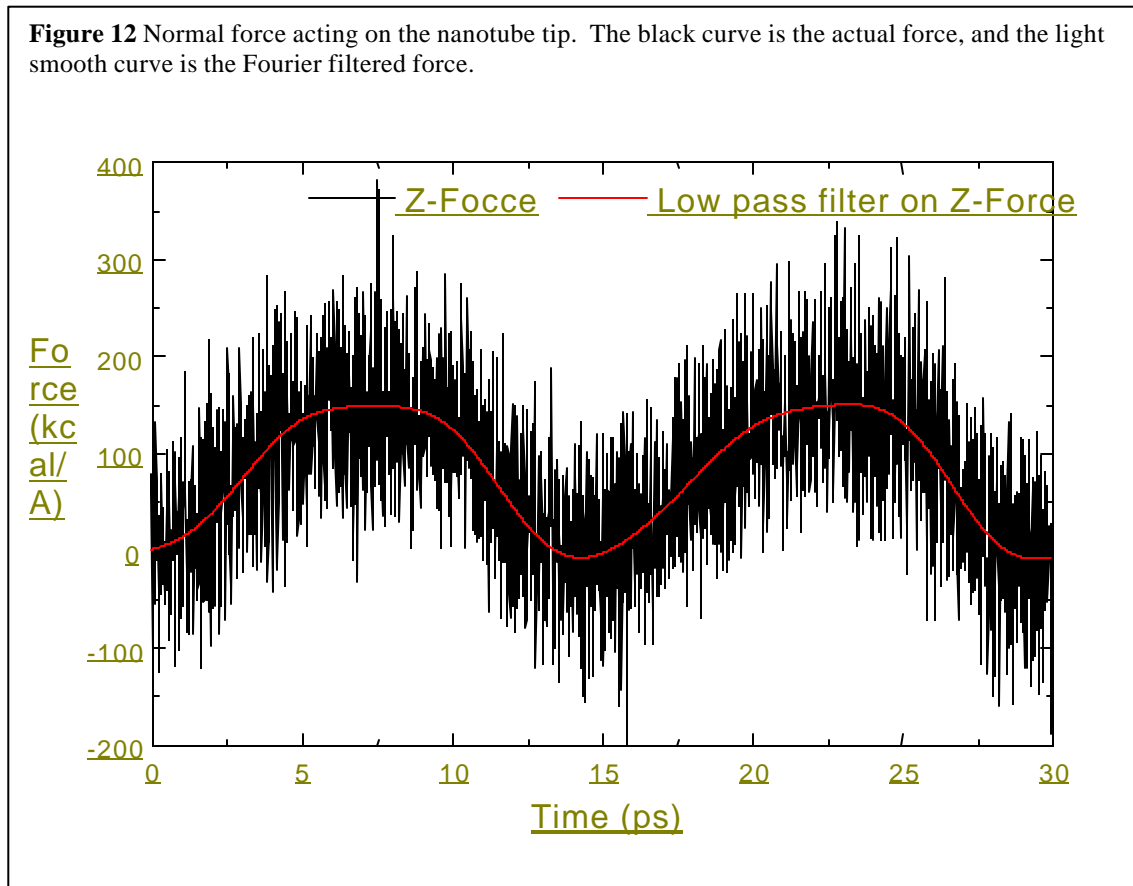


Figure 13 Lateral forces on the nanotube tip. The dark curves are the actual forces, and the lighter smoothed curves are Fourier filtered forces

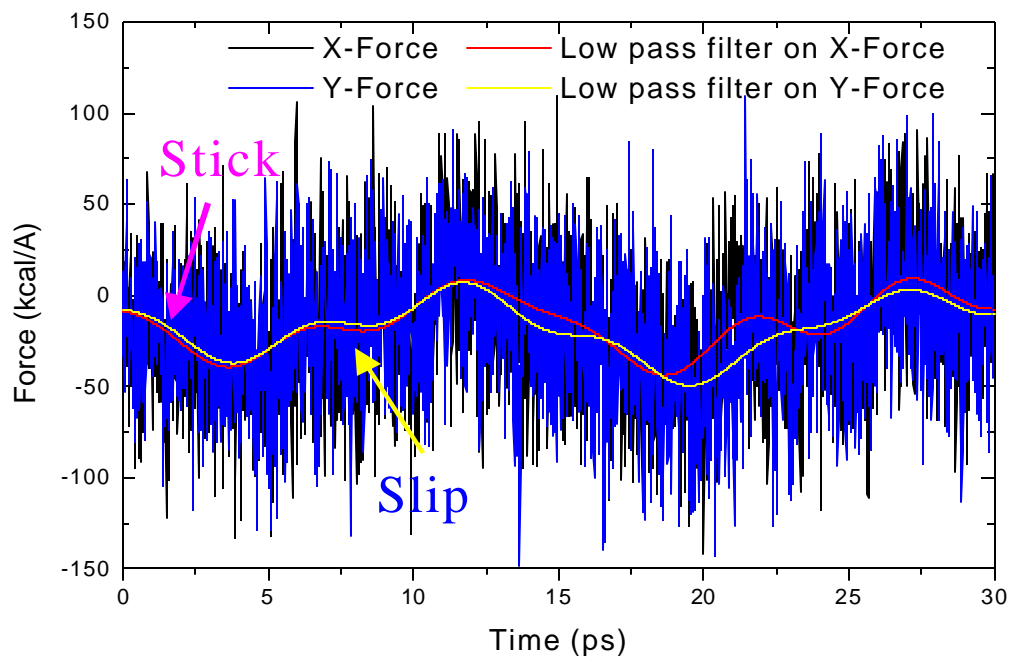
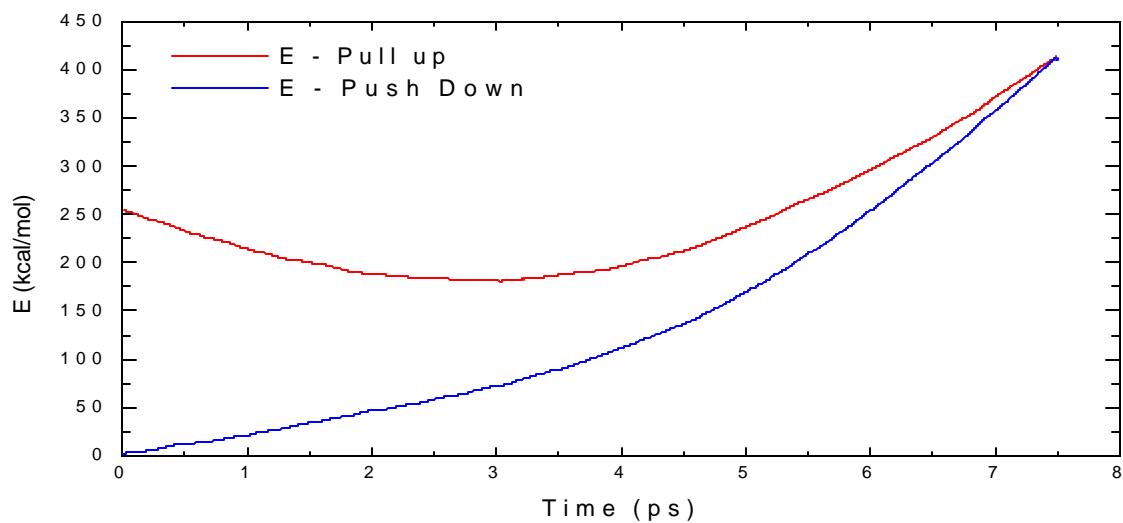


Figure 14 Energy dissipation due to friction between diamond surface and nanotube tip



6. Summary

We have presented methods to obtain a fundamental understanding of the physico-chemistry of sliding systems in contact that underlies the materials science and mechanics issues essential to tribology. Advances in theory and methods are now making it practical to consider fully first principles (de novo) predictions of surface and interface structures and their role in determining tribological properties of materials..

We illustrated the atomistic approach to tribology of metal surfaces by determining the shear and friction for Ni(001)/Ni(001) as a function of misorientation. These results suggest that some degree of plasticity occurs even for careful experiments on clean samples.

We also presented the use of NEMD to study the rheology of confined lubricants, considering a system of two oxidized iron surfaces, covered with DTP wear inhibitors, and lubricated with hexadecane. These results illustrate the dramatic effects of nanoconfinement. We illustrate the use of bond dissociation consistent FF, by examining the use of nanotubes as nanotribological probes.

Acknowledgments

This research was supported by a NASA Grant for Computational Nanotechnology, a NASA-JPL TCA grant involving collaboration with Hughes and Raytheon, and a contract with Chevron Chemical Company (Oronite Technology group). The authors would like to thank Dr Gelmann for early preprint of their paper, and thanks to Dr. M. Gardos (Raytheon) and Dr. Y.T. Chen (of GM) for fruitful discussions. The development of the methodologies used in this work was supported by grants from the DOE-ASCI-ASAP and NSF (CHE 95-12279 and MRI 99-xxxxx). The facilities of the MSC used in this research are also supported by grants from ARO-DURIP, ARO-MURI, Beckman Institute, Seiko-Epson, Avery-Dennison Corp., 3M, Dow, Kellogg, GM, Chevron Research Technology Co. and Asahi Chemical.

REFERENCES

1. W. A. Goddard III, T. H. Dunning Jr., W. J. Hunt and P. J. Hay, *Accts. Chem. Res.* **6**, 368 (1973)
2. D. J. Tannor, B. Marten, R. Murphy, R. A. Friesner, D. Sitkoff, A. Nicholls, M. Ringnald, W. A. Goddard III, and B.

- Honig, *J. Am. Chem. Soc.* **116**, 11875 (1994)
3. B. H. Greeley, T. V. Russo, D. T. Mainz, R. A. Friesner, J-M. Langlois, W. A. Goddard III, R. E. Donnelly, and M. N. Ringnald, *J. Chem. Phys.* **101**, 4028 (1994).
4. X. J. Chen, J-M. Langlois, and W. A. Goddard, *Phys. Rev. B* **52**, 2348 (1995)
5. A. Strachan, T. Cagin, W. A. Goddard, III, *Phys. Rev. B* **60**, 15084 (1999);
6. A. Strachan, T. Cagin, O. Gulseren, R. E. Cohen, and W. A. Goddard, III, "qEAM FF for Tanatalum," submitted to *Phys. Rev. B*;
7. S. Dasgupta, T. Yamasaki, and W. A. Goddard III, *J. Chem. Phys.* **104**, 2898 (1996)
8. N. Karasawa, S. Dasgupta, and W. A. Goddard III, *J. Phys. Chem.* **95**, 2260 (1990)
9. S. Dasgupta, W. B. Hammond, and W. A. Goddard III, *J. Am. Chem. Soc.*, **118**, 12291-12301 (1996).
10. N. Karasawa and W. A. Goddard III, *Macromolecules* **28**, 6765 (1995)
11. N. Karasawa and W. A. Goddard III, *Macromolecules* **25**, 7268 (1992)
12. S. Dasgupta, K.A. Brameld, C. F. Fan and W. A. Goddard, *Spect. Acta. A* **53**, 1347-1363 (1997).
13. S. Dasgupta, K. A. Smith, and W. A. Goddard III, *J. Phys. Chem.* **97**, 10891 (1993)
14. J. A. Wendel and W. A. Goddard III, *J. Chem. Phys.* **97**, 5048 (1992)
15. C. B. Musgrave, S. Dasgupta, and W. A. Goddard III, *J. Phys. Chem.* **99**, 13321 (1995)
16. C. B. Musgrave, S. J. Harris, and W. A. Goddard III *Chem. Phys. Lett.* **247**, 359 (1995)
17. M. McAdon and W. A. Goddard, III, *J. Phys. Chem.* **91**, 2607 (1987).
18. S. L. Mayo, B. D. Olafson, and W. A. Goddard III, *J. Phys. Chem.* **94**, 8897 (1990).
19. A. K. Rappé, C. J. Casewit, K. S. Colwell, W. A. Goddard III, and W. M. Skiff, *J. Am. Chem. Soc.* **114**, 10024 (1992)
20. T. Cagin, Y. Qi, H. Li, Y. Kimura, H. Ikeda, W. L. Johnson, and W. A. Goddard, III, *Bulk Metallic Glasses*, eds. A. Inoue, W. L. Johnson, C. T. Liu, *MRS Symp. Ser.* **554**, 43-48 (1999);
21. Y. Kimura, T. Cagin, Y. Qi and W. A. Goddard, III, *Phys. Rev. B*, submitted.
22. T. Cagin, E. Demiralp, and W. A. Goddard, III, *MRS Symp. Proc. Vol* **492**, (1998) 287-

- 292.;
23. E. Demiralp, T. Cagin and W. A. Goddard, *Phys. Rev. Lett.* **82**, 1708-1711 (1999);
 24. N. T. Huff, E. Demiralp, T. Cagin and W. A. Goddard, III, *J. Noncrystal. Solids* **253**, 133-142 (1999);
 25. O. Kitao, E. Demiralp, T. Cagin, S. Dasgupta, M. Mikami, K. Tanabe, S. Ono, W. A. Goddard III, *Comput. Mat. Sci.* **14**, 135-138 (1999).
 26. J. W. Che, T. Cagin, W. A. Goddard, III, *Theo. Chem. Acct.* **102**, 346-354 (1999);
 27. A. Duin and W. A. Goddard, III to be submitted,
 28. T. Cagin and J. R. Ray, *Phys. Rev. A* **37**, 247 (1988); T. Cagin and J. R. Ray, *Phys. Rev. A*, **37**, 4510 (1988); T. Cagin and J. R. Ray, *Phys. Rev. B* **37**, 699 (1988).
 29. T. Cagin and J. R. Ray, *Phys. Rev. B*, **38**, 7940 (1988); T. Cagin and B. M. Pettitt, *Phys. Rev. B* **39**, 12484 (1989)
 30. N. Karasawa and W. A. Goddard III, *J. Phys. Chem.* **93**, 7320 (1989)
 31. Z. M. Chen, T. Cagin and W. A. Goddard, III, *J. Comp. Chem.* **18**, 1365 (1997).
 32. H. Q. Ding, N. Karasawa and W. A. Goddard III, *J. Chem. Phys.* **97**, 6 (1992)
 33. Lim, K.T., Brunett, S., Iotov, M., McClurg, R.B., Vaidehi, N., Dasgupta, S., Taylor, S. and Goddard III, W.A. (1997) *J. Comp. Chem.* **18**, 501-521.
 34. M. Iotov, S. Kashihara, S. D. Dasgupta, W. A. Goddard, III, "Diffusion of Gases in Polymers", unpublished; M. Iotov, Ph. D. Thesis, California Institute of Technology, December 1997.
 35. P. Miklis, T. Cagin, and W. A. Goddard III, *J. Am. Chem. Soc.* **119**, 7458 (1997).
 36. H. Ding, N. Karasawa, and W. A. Goddard III, *Chem. Phys. Lett.* **196**, 6 (1992)
 37. A. M. Mathiowetz, A. Jain, N. Karasawa, and W. A. Goddard III *Proteins* **20**, 227 (1994)
 38. N. Vaidehi, A. Jain, and W. A. Goddard III, *J. Phys. Chem.* **100**, 10508 (1996).
 39. A. Fijany, T. Cagin, A.J-Botero, and W. A. Goddard, III, *Adv. Eng. Software*, **29**, 441-450 (1998).
 40. A. Fijany, A. J-Botero, T. Cagin, in *Parallel Computing: Fundamentals, Applications and New Directions*, Eds. D'Hollander, G. Joubert, F. Peters, and U. Trottenberg, 505-515 (1998).
 41. T. Cagin, N. Karasawa, S. Dasgupta, and W. A. Goddard III, *Mat. Res. Soc. Symp. Proc.* **278-283** (1992)
 42. T. Cagin, W. A. Goddard III, and M. L. Ary, *Comp. Polymer Sci.* **1** (1991) 241.
 43. M. Parrinello and A. Rahman, *Phys. Rev. Lett.* **45**, 1196 (1980); M. Parrinello and A. Rahman, *J. Appl. Phys.* **52**, 7182 (1981).
 44. S. Nose, *Mol. Phys.* **52**, 255 (1984); S. Nose, *J. Chem. Phys.* **81**, (1984) 511.
 45. T. Cagin and B. M. Pettitt, *Mol. Phys.* **72**, 111 (1991); T. Cagin and B. M. Pettitt, *Mol. Simul.* **5**, 1 (1991)
 46. Yue Qi, T. Cagin. Y. Kimura, W. A. Goddard III, "Shear Viscosity of a Liquid Metal Alloy from NEMD: Au-Cu", unpublished.
 47. Jianwei Che, Tahir Cagin, and W. A. Goddard, III, *Nanotech.* **11**, 65-69 (2000)
 48. J. Che, T. Cagin, W. Deng, W. A. Goddard, III, "Thermal Conductivity Studies by Molecular Dynamics Simulations," *J. Chem. Phys.* **113** (2000).
 49. T. Cagin, P. Miklis, and W. A. Goddard, III, "Effect of molecular topology on the shear viscosity: linear, star and hyper-branched alkanes," in preparation.
 50. T. Cagin, J. Che, M. N. Gardos, A. Fijany, and W. A. Goddard, III, *Nanotech.* **10**, 278-284 (1999).
 51. T. Cagin, Y. Zhou, E. S. Yamaguchi, R. Frazier, A. Ho, Y. Tang, and W. A. Goddard III, in *Dynamics in Small Confining Systems V*, MRS Symp. Ser. **543**, 79-84 (1999). Eds. J. M. Drake, G. S. Grest, J. Klafter, and R. Kopelman; Y.
 52. Y. Zhou, T. Cagin, E.S. Yamaguchi, A. Ho, R. Fraszier, Y-C Tang, W. A. Goddard, III, in *Theory of Electrochemical Interfaces*, Ed. Woods Hailey.
 53. J. S. Ko and A. J. Gellman, "Friction anisotropy at Ni(100)/Ni(100) interface," *Langmuir*, submitted.
 54. Y. I. Frenkel and T. Kontorova, *JETP*, **8**, 1340 (1938); K. Shinjo and M. Hirono *Surf. Sci.* **283**, 273 (1993)
 55. M. O. Robbins and E. D. Smith, *Langmuir* **12**, 4543 (1996); G. He M. H. Muser, M. O. Robbins, *Science* **284**, 1650 (1999)
 56. J. R. Smith, G. Bozzolo, A. Banjera, and J. Ferrante, *Phys. Rev. Lett.* **63**, 1269 (1989)
 57. Y. Qi, T. Cagin and W. A. Goddard, III, *Phys. Rev. B* **59**, 3527-3533 (1999)
 58. H. Ikeda, Y. Qi, T. Cagin, K. Samwer, W.L. Johnson, W. A. Goddard, III, *Phys. Rev. Lett.* **82**, 2900 (1999).
 59. Y. Qi, H. Ikeda, T. Cagin, K. Samwer, W. L. Johnson, W. A. Goddard, III, in *Bulk Metallic Glasses*, Eds. A. Inoue, W. L.

- Johnson, C. T. Liu, 367-372 (1999).
60. B. Bhushan, J. N. Israelachvili, U. Landman, *Nature*, **1995**, **374**, 607)
 61. Thompson, P. A.; Troian, S. M. *Nature*, **1997**, **389**, 360.
 62. Granick, S. *Science*, **1991**, **253**, 1374.
 63. Yoshizawa, H.; Israelachvili, J. N. *J. Phys. Chem.*, **1993**, **97**, 11300.
 64. Georges, J. M.; Tonick, A., Poletti; S., Yamaguchi, E. S.; Ryason, P. R. *Trib. Trans.* **1998**, **41**, 543.
 65. Jiang, S.; Dasgupta, S.; Blanco, M.; Frazier, R.; Yamaguchi, E. S.; Tang, Y., Goddard, W. A., III *J. Phys. Chem.* **1996**, **100**, 15760.
 66. Jiang, S.; Frazier, R.; Yamaguchi, E. S.; Blanco, M.; Dasgupta, S.; Zhou, Y.; Cagin, T.; Tang, Y.; and Goddard, W. A., III *J. Phys. Chem. B*, **1997**, **101**, 7702.
 67. Zhou, Y.; Jiang, S.; Cagin, T.; Yamaguchi, E. S.; Frazier, R.; Ho, A.; Tang, Y., Goddard, W. A., III, *J. Phys. Chem. A*, **2000**, **104**, 2508.
 68. Zhou, Y.; Cagin, T.; Yamaguchi, E. S.; Frazier, R.; Ho, A.; Tang, Y., Goddard, W. A., III "Dynamical Shear Studies of Nanoscale Lubricant Films Confined Between Iron Oxide Surfaces Covered with DTP Wear Inhibitors". *J. Phys. Chem.*, **2000**, submitted.
 69. Rhykerd, C. L. Jr.; Schoen, M.; Diestler, D. J.; Cushman, J. H. *Nature*, **1987**, **330**, 461. Stevens, M. J.; Mondello, M.; Grest, G. S.; Cui, S. T.; Cochran, H. D.; Cummings, P. T. *J. Chem. Phys.*, **1997**, **106**, 7303
 70. Yoshizawa, H.; Chen, Y. L; Israelachvili, J. N. *J. Phys. Chem.*, **1993**, **97**, 4128.